Check for updates

ADVANCED ENERGY MATERIALS
www.advenergymat.de

To Be or Not to Be – Is $MgSc_2Se_4$ a Mg-Ion Solid Electrolyte?

*Clarissa Glaser, Zhixuan Wei, Sylvio Indris, Philip Klement, Sangam Chatterjee, Helmut Ehrenberg, Zhirong Zhao-Karger, Marcus Rohnke, and Jürgen Janek**

Magnesium batteries offer promising potential as next-generation sustainable energy-storage solutions due to the high theoretical capacity of the magnesium metal anode. Facilitating dendrite-free operation of metal anodes necessitates the development of solid electrolytes with high magnesium-ion conductivity. While the chalcogenide spinel $MgSc_2Se_4$ is predicted to exhibit high magnesium ion mobility, unequivocal experimental evidence for magnesium ion conduction beyond short-range motion is still missing. This study confirms magnesium-ion transport in $MgSc_2Se_4$ through two independent electrochemical methods: electrochemical deposition of magnesium metal and reversible magnesium plating/stripping cycling. To overcome the difficulty of measuring the ionic conductivity of the mixed conducting $MgSc_2Se_4$ spinel, a pure ion conducting interlayer is employed in a symmetric transference cell. This approach effectively suppresses the electron transport, allowing accurate characterization of the ionic conductivity. The experimental results confirm a low migration barrier of (386 ± 24) meV for magnesium ion transport in $MgSc_2Se_4$ and demonstrate one of the best performances at room temperature among the reported inorganic magnesium solid electrolytes. The findings open a new door for exploring additional mixed magnesium ion conductors and highlight the potential of magnesium chalcogenide spinels as a promising class of magnesium solid electrolytes.

1. Introduction

Lithium-ion batteries (LIBs) have emerged as the most promising energy storage systems for portable and smart electronic devices.[1] However, the limited lithium availability and safety issues of LIBs combined with the growth of the human demand for energy increased the interest in developing next-generation battery cells.[2–4] Recently, sodium-ion batteries (SIB) have emerged as a serious new storage concept, with commercialization efforts already underway.[5] While potassium ion cells may appear as a natural progression, cell concepts utilizing multivalent ions such as Mg^{2+}, Ca^{2+} and Zn^{2+} offer the potential for higher volumetric energy densities compared to cells utilizing monovalent ions. Furthermore, these multivalent ion-based cells are expected to achieve lower cost, making them an attractive option.[6] As a result, research activity on calcium and zinc has grown rapidly, albeit not to the same extent as magnesium. The discrepancy is probably due to the fact that the suitability of calcium and zinc as safe anode materials has not been studied as extensively. In alkaline aqueous solutions, zinc notoriously plates into tree-like dendrites, while calcium exhibits various morphologies, including the desired dense and thick bulk structures that are widely documented for magnesium.[3] In addition to this, magnesium-ion batteries (MIBs) are an attractive avenue for further development alongside the alkali-ion technology. This is primarily due to the outstanding characteristics of the magnesium metal anode, which include an almost

C. Glaser, Z. Wei, M. Rohnke, J. Janek
Institute of Physical Chemistry
Justus Liebig University Giessen
Heinrich-Buff-Ring 17, D-35392 Giessen, Germany
E-mail: Juergen.Janek@phys.chemie.uni-giessen.de

C. Glaser, Z. Wei, P. Klement, S. Chatterjee, M. Rohnke, J. Janek
Center for Materials Research (ZfM)
Justus Liebig University Giessen
Heinrich-Buff-Ring 16–17, D-35392 Giessen, Germany

S. Indris, H. Ehrenberg
Institute for Applied Materials - Energy Storage Systems (IAM-ESS)
Karlsruhe Institute of Technology (KIT)
Hermann-von-Helmholtz-Platz 1, D-76344 Eggenstein-Leopoldshafen, Germany

P. Klement, S. Chatterjee
Institute of Experimental Physics I
Justus Liebig University Giessen
Heinrich-Buff-Ring 16, D-35392 Giessen, Germany

Z. Zhao-Karger
Institute of Nanotechnology (INT)
Karlsruhe Institute of Technology (KIT)
Hermann-von-Helmholtz-Platz 1, D-76344 Eggenstein-Leopoldshafen, Germany

Z. Zhao-Karger
Helmholtz Institute Ulm (HIU) Electrochemical Energy Storage
Helmholtzstrasse 11, D-89081 Ulm, Germany

The ORCID identification number(s) for the author(s) of this article can be found under https://doi.org/10.1002/aenm.202301980

© 2023 The Authors. Advanced Energy Materials published by Wiley-VCH GmbH. This is an open access article under the terms of the Creative Commons Attribution-NonCommercial-NoDerivs License, which permits use and distribution in any medium, provided the original work is properly cited, the use is non-commercial and no modifications or adaptations are made.

DOI: 10.1002/aenm.202301980

16146840, 2023, 40, Downloaded from https://onlinelibrary.wiley.com/doi/10.1002/aenm.202301980 by Cochrane Germany, Wiley Online Library on [07/12/2023]. See the Terms and Conditions (https://onlinelibrary.wiley.com/terms-and-conditions) on Wiley Online Library for rules of use; OA articles are governed by the applicable Creative Commons License

double volumetric capacity of q_V = 3833 mAh cm^{-3} and 10^4 times higher earth-abundance compared to lithium, and a low potential of magnesium (E_H = −2.37 V vs SHE). Furthermore, the Mg metal anode is predicted to be less reactive and less prone to dendrite formation, making MIBs a more secure energy storage option.[2,7] Despite these theoretical advantages of magnesium, there are several key challenges that need to be addressed in the development of electrolytes and cathodes before MIBs can be practically implemented. The knowledge gained from the research on LIBs and SIBs cannot be directly transferred to MIBs due to the significant differences in the electrochemistry of monovalent and multivalent ions in various aspects. For instance, an ion-blocking passivation layer forms on Mg metal when it comes into contact with conventional carbonate-based electrolyte solvents that are widely used in LIBs and SIBs.[8,9] Consequently, novel electrolytes based on Grignard reagents have been developed. However, safety concerns associated with their ether-based solvents, such as high vapor pressure and flammability, arise.[9,10] Alternatively, non-flammable ionic liquids (ILs) can be used as solvents to dissolve magnesium salts, provided that they possess a sufficient reductive stability against the Mg metal.[7] In light of this, solid electrolytes (SEs) can be viewed as a safe alternative, where the most challenging factor is to achieve sufficient conductivity at room temperature due to the typically low ion mobility resulting from the high charge density of the Mg^{2+} ion.[10]

The earliest work on Mg-ion SEs dates back to 1987, when Ikeda et al. reported an ionic conductivity of σ_{ion} = 6×10^{-3} S cm^{-1} at 800 °C for $Mg_{0.5}Zr_2(PO_4)_3$.[11] The conductivity at room temperature is ten orders of magnitude lower. To improve the room temperature conductivity, several studies on the substitution of aliovalent ions on the Zr- and P-lattice sites have been performed. However, so far the reported conductivities are still limited to values below $\sigma_{ion} = 3 \times 10^{-5}$ S cm^{-1}.[12] Borohydrides, another class of Mg-ion conductors, benefit from the Mg-ion zigzag chains in the tunneling crystal structure that allows fast Mg-ion diffusion. Recently, the nanocomposite $Mg(BH_4)_2$·1.5THF-MgO(75 wt%) achieved an ionic conductivity of $\sigma_{ion} \approx 10^{-4}$ S cm^{-1} at mildly elevated temperature of 70 °C. However, the presence of inactive MgO, which is necessary for mechanical stabilization, limits the ionic conductivity of the material.[13] Therefore, in order to improve conductivity and stability, and expand the operating potential window, additional modifications are necessary.[10] In addition to these materials, Yamanaka et al. synthesized MgS-P_2S_5-MgI_2[14], a sulfide-based SE analogous to the lithium SE found in the quasi-binary and -ternary systems Li_2S-P_2S_5 and Li_2S-P_2S_5-LiX (X = Cl, Br, I).[15] The glass-ceramic SE achieved an ionic conductivity of $\sigma_{ion} = 2 \times 10^{-7}$ S cm^{-1} at 200 °C as the framework was expanded by the large iodine anions. However, there is still a need for optimization strategies to further improve the performance.

The computational studies of Canepa et al., which predict low migration barriers (0.36–0.53 eV) in MgZ_2X_4 (Z = In, Y, Sc and X = S, Se) spinel chalcogenides, can be considered as a major breakthrough in the search for inorganic Mg-ion SEs.[16] In the spinel structure (**Figure 1**a), the Mg-ions occupy an unfavorable tetrahedrally coordinated stable site (*tet*) and hop across a favorable octahedral activated site (*oct*) to reach the next tetrahedral site along the migration path. Thereby, the magnitude of the migration barrier is determined by the shared triangular face (*tri*) between tetrahedra and octahedra, namely the bottleneck of the energy landscape, which can be widened by increasing the volume per anion. After successful synthesis of one of the spinels, $MgSc_2Se_4$, Canepa et al. performed ^{25}Mg static variable temperature spin lattice relaxation nuclear magnetic resonance (SLR NMR) measurements and determined a Mg^{2+} migration barrier of (370 ± 90) meV, consistent with their computed data. However, this experimental evidence of Mg^{2+} mobility only corresponds to short-range motion/local jumps, while the long-range motion is of particular importance for the electrochemical performance of a solid electrolyte. Hence, they carried out impedance measurements with ion-blocking Ta electrodes and estimated an ionic conductivity of $\approx 1 \times 10^{-4}$ S cm^{-1} at room temperature. In their equivalent circuit, two Jamnik-Maier elements were utilized,[17] representing bulk and grain boundary contributions in the high frequency range. The total ionic resistance was determined by the Re(Z) axis intercept at the offset of the observed semicircle. However, we consider the results are yet not sufficiently evident due to lack of data points in the high-frequency range, which are necessary for accurately determining the intercept and obtaining a satisfactory fit of the spectrum (see Figure S1, Supporting Information). We consider it fortuitous as that the evaluated conductivity coincides with the true conductivity. However, from a critical perspective, the reported impedance data do not provide clear evidence for Mg-ion conduction in the $MgSc_2Se_4$ spinel. The authors determined an electronic conductivity of $\sigma_{el} = 4 \times 10^{-8}$ S cm^{-1}, which could potentially be attributed to point defects, neutralized by electrons, or the presence of electron conducting secondary phases. This high electronic conductivity poses a challenge for its practical application as it leads to significant self-discharge.[16] In our earlier work, we estimated the self-discharge for a charged $Mg|MgSc_2Se_4|Mo_6S_8$ battery and found that 10% of the total charge capacity would be lost within a short duration of 16 h.[18] Due to the promising ionic conductivity of $MgSc_2Se_4$ reported by Canepa et al., follow-up works have been carried out to gain a more comprehensive understanding. Wang et al. employed two routes of compositional tuning to suppress the electronic conductivity of $MgSc_2Se_4$, but neither method was successful.[19] It is worth mentioning that the impedance analysis by both, Wang et al. and by Canepa et al., is unreliable. In their work, Kundu and co-workers focused more on the synthesis parameters. On one hand, they proposed avoiding high energy precursor ball milling before the solid-state reaction since it can cause the formation of an electron conducting ScSe phase.[20] On the other hand, they reported an electric field-assisted synthesis route, including a subsequent low thermal treatment (500 °C for 40 h), to obtain a more phase pure spinel with less electron conducting impurity phases. Given the doubts surrounding the impedance analysis by both, Canepa et al. and Wang et al., it is crucial to prioritize the definitive verification of the partial ionic conductivity of $MgSc_2Se_4$ as prototype Mg-ion conducting spinel. This step is essential before spending more efforts to reduce the partial electronic conductivity. We like to add that the well-established strategies to determine the partial ionic conductivity of mixed ionic/electronic conductors (electrolysis method,[21] emf of galvanic cells,[21,22] 4-point stationary polarization method[21,23]) are not applicable

© 2023 The Authors. Advanced Energy Materials published by Wiley-VCH GmbH

due to the lack of suitable and compatible electrodes with low overpotential. In view of all these challenges, it is the key target of this work to demonstrate unequivocally the relatively high Mg-ion conductivity of the $MgSc_2Se_4$ spinel, even over a long range.

To address this challenge, we successfully synthesized nearly phase pure $MgSc_2Se_4$ using a solid-state synthesis in a quartz glass ampule. We present reliable evidence for Mg-ion conduction in $MgSc_2Se_4$ through an electrochemical Mg plating experiment. Furthermore, we establish a universally applicable procedure to determine the partial ionic conductivity of the spinel. The Mg-ion migration barrier E_a results as (386 ± 24) meV, determined through temperature-dependent impedance measurements using the same electrochemical cell. We anticipate that these findings will advance the research on $MgSc_2Se_4$ and pave the way for exploring other mixed conducting MgZ_2X_4 spinels as potential Mg-ion solid electrolytes.

2. Results and Discussion

2.1. Structure and Morphology Information of $MgSc_2Se_4$

$MgSc_2Se_4$ powder was prepared via one- and two-step solid-state reaction routes. By performing Rietveld refinement based on the X-ray diffraction (XRD) data of both types of $MgSc_2Se_4$ samples (Figure 1a; Figure S2, Supporting Information), we identified a cubic spinel structure within the Fd-3m space group, where the Mg-ions are positioned on the 8*b* sites (tetrahedra), while the 16*c* sites (octahedra) are occupied by the Sc-ions for both samples. The detailed crystallographic data of these refinements, which are in good agreement with previously published results by Canepa et al.[16] and Wang et al.,[19] can be found in the Tables S1 and S2 (Supporting Information). Furthermore, the refined data confirm almost phase pure samples with a comparably small fraction of MgSe impurity (4.4 and 5.1 wt% for one-step and two-step synthesis, respectively). Since the one-step synthesized $MgSc_2Se_4$ shows slightly higher purity, it was chosen for all subsequent investigations. From the additional characterization by energy-dispersive X-ray spectroscopy (EDS) during scanning electron microscopy (SEM) measurements, as shown in Figure 1b, uniform distributions of the elements Mg, Sc, and Se were obtained. The atomic ratio of 1:2.3:3.6 confirms the spinel stoichiometry, whereby the small deficit of Mg and Se is due to vapor loss from the pellet surface at the high synthesis temperature. In addition to the particle size in the agglomerates indicated by the SEM image (1–5 µm), transmission electron microscopy (TEM) images (Figure S3a,b, Supporting Information) also demonstrate that the as-prepared $MgSc_2Se_4$ shows a typical particle size from 1–3 µm. Furthermore, the selected area electron diffraction (SAED) pattern performed during TEM measurements confirms the spinel structure as well (diffraction image depicted in Figure S3c, Supporting Information). To obtain information on the Mg and Sc positions in the sample, ^{25}Mg and ^{45}Sc magic-angle spinning nuclear magnetic resonance (MAS NMR) spectroscopy was carried out (see Figure 1c,d). The ^{25}Mg MAS NMR spectrum shows a single peak at 53.2 ppm, which agrees with the results of Canepa et al., indicating the presence of Mg exclusively on the tetrahedral sites. The strong peak at 429 ppm in the ^{45}Sc MAS NMR spectrum confirms the presence of Sc predominantly on the octahedral sites, while the small peak at 400 ppm (area fraction 1.3%) might arise from a secondary phase or from a small fraction of Sc-ions on the tetrahedral sites. The latter is quite likely, since the sample shows a Sc excess according to the EDS results. This excess Sc tends to occupy Mg sites, forming the $Sc^{\bullet}_{Mg}$ anti-site defect (n-type defect) which is probably charge-balanced by electrons.[24] These can cause increased electronic conductivity when the conduction band minimum is reached in terms of energy. The semiconducting nature of $MgSc_2Se_4$, as suggested in the literature,[25] is confirmed through absorption and photoluminescence spectroscopy. Linear absorption measurements (Figure 1e) yield a band-gap energy of E_g = 2.3 eV, and a direct allowed transition by the Tauc method (Figure 1f). This is consistent with the light-brown translucent appearance of the samples (Figure 1b). Additionally, a much more prominent absorption band is observed at higher energies, with a second absorption edge around $E_{g'}$ = 2.8 eV, in agreement with previous reports of a band-gap energy of approximately 3 eV for the corresponding sulfide-based spinel $MgSc_2S_4$.[26] Furthermore, $MgSc_2Se_4$ exhibits a spectrally broad photoluminescence centered at 1.93 eV and a full width at half maximum (FWHM) of 0.44 eV. Notably, the photoluminescence is Stokes-shifted by 0.37 eV from the absorption edge. These findings provide further evidence for the semiconducting nature of $MgSc_2Se_4$.

2.2. Electronic Conductivity

The room temperature partial electronic conductivity of the semi-conductor $MgSc_2Se_4$ was determined by electrochemical impedance spectroscopy (EIS) and chronoamperometry (CA) measurements. In both cases, symmetric cells (Me|$MgSc_2Se_4$|Me) with ion-blocking metal (Me) electrodes were used. Initially, to find out the best cell configuration, Nyquist plots using different ion-blocking electrodes (stainless-steel punches (SS), Ta foil and Au foil) were compared. For this purpose, homemade press cells were used,[28] consisting of a PEEK housing in which the $MgSc_2Se_4$ powder was pressed in between two stainless-steel punches, with the punches serving directly as ion-blocking electrodes. In the case of Ta or Au blocking electrodes, the metal foils were subsequently placed between the cold-pressed $MgSc_2Se_4$ pellet and the stainless-steel punches. As shown in Figure S4 (Supporting Information), application of this cold-pressing procedure with ion-blocking electrodes results in noisy impedance spectra, which can be attributed to poor physical contact at the electrode|SE interface. Among them, the Au foil comparatively shows the best physical contact, and a semicircle was detected in the Nyquist plot. To further improve the contact, with the consideration that foils are mostly stiff and therefore difficult to adapt to bumps on the rough SE surface, a smoothing Au layer was evaporated onto both sides of a sintered spinel pellet. Then, the pellet was placed between Ni arrestors as current collectors in a pouch cell and the EIS measurements were performed again. As can be seen in the corresponding Nyquist plot in **Figure 2**a, the gas phase deposition significantly improves the physical contact. A noiseless spectrum results, showing a characteristic depressed semicircle without low-frequency tail. The missing tail may be explained by an imperfect ion-blocking electrode. An ideal ion-blocking

© 2023 The Authors. Advanced Energy Materials published by Wiley-VCH GmbH

16146840, 2023, 40, Downloaded from https://onlinelibrary.wiley.com/doi/10.1002/aenm.202301980 by Cochrane Germany, Wiley Online Library on [07/12/2023]. See the Terms and Conditions (https://onlinelibrary.wiley.com/terms-and-conditions) on Wiley Online Library for rules of use; OA articles are governed by the applicable Creative Commons License

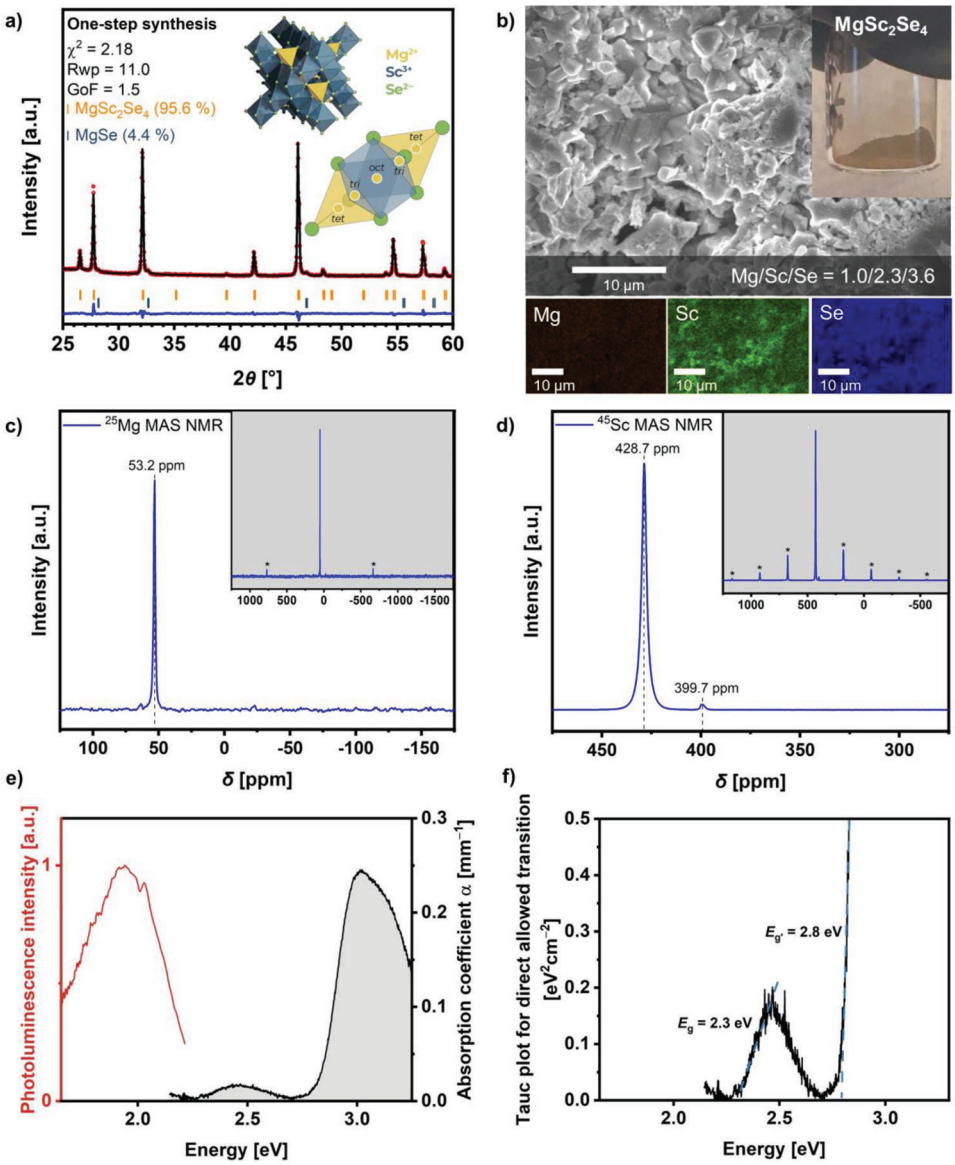

Figure 1. a) Rietveld refinement, based on the XRD pattern for one-step synthesized $MgSc_2Se_4$. The observed and calculated curves are shown in red and black in the top, and the difference curve is shown in blue. The inset in the right upper corner shows the crystal structure of $MgSc_2Se_4$ and the diffusion path for Mg^{2+}, as described by Guittard et al.;[27] b) SEM image of $MgSc_2Se_4$, photographic image of the $MgSc_2Se_4$ powder and EDS mapping of the elements Mg, Sc and Se; characterization of Mg and Sc positions in the spinel structure via c) ^{25}Mg solid-state NMR and d) ^{45}Sc solid-state NMR. Spinning sidebands are marked with an asterisk; e) absorption (black line) and photoluminescence (red line) of $MgSc_2Se_4$ and f) Tauc plot.

electrode should be inert and not form an alloy with magnesium. This is not as simple as for Li-ion and Na-ion conductors, where several working examples exist.[29] Nevertheless, the partial electronic conductivity σ_{el} can be calculated from the intercept of the Nyquist plot with the real axis at low frequency, i.e., from the electronic resistance R_{el}, in the impedance spectrum of an Au|$MgSc_2Se_4$|Au pouch cell (Figure 2a) by using the following equation (Equation 1):

$$\sigma_i = \frac{d}{A\,R_i} \quad (i = el,\ ion,\ tot) \tag{1}$$

A is the contact area of a deposited Au electrode (0.503 cm^2), d is the thickness of the pellet (0.130 cm), and R_i is the electronic (el), ionic (ion), or total (tot) resistance. Since the large overlap of the two transport contributions (ionic and electronic) makes it difficult to obtain a reliable analysis using equivalent circuits,[30] including those used in literature,[16,19] R_{el} was extracted from the last data point at low frequency. As a result, σ_{el} was calculated to be 3.4×10^{-8} S cm^{-1} at room temperature, which can also be confirmed by the dc polarization measurement ($\sigma_{el} = 2.1 \times 10^{-8}$ S cm^{-1}), shown in Figure 2b, in accordance with the results from the groups of Ceder and Fichtner.[16,19] The electronic conductivity, which is even around twice as high at an elevated temperature

© 2023 The Authors. Advanced Energy Materials published by Wiley-VCH GmbH

16146840, 2023, 40, Downloaded from https://onlinelibrary.wiley.com/doi/10.1002/aenm.202301980 by Cochrane Germany, Wiley Online Library on [07/12/2023]. See the Terms and Conditions (https://onlinelibrary.wiley.com/terms-and-conditions) on Wiley Online Library for rules of use; OA articles are governed by the applicable Creative Commons License

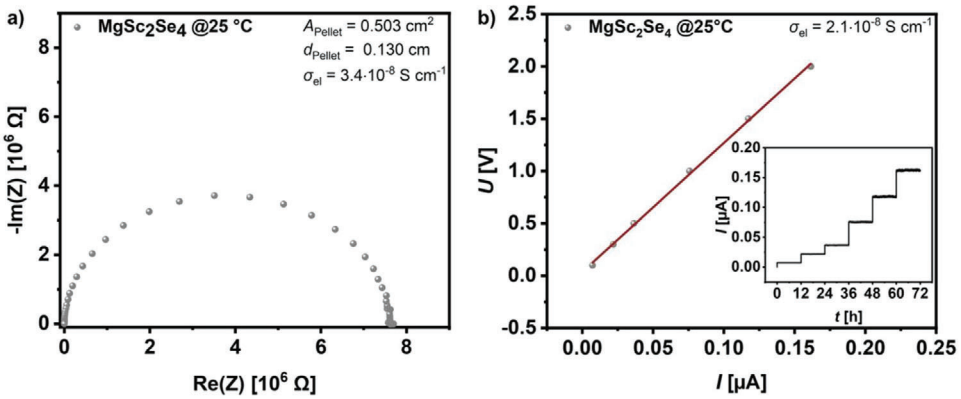

Figure 2. a) Nyquist plot of an Au|$MgSc_2Se_4$|Au pouch cell in the frequency range of 7 MHz to 100 mHz at 25 °C and b) DC polarization data obtained at different voltages (0.1, 0.3, 0.5, 1.0, 1.5 and 2.0 V, held for 12 h, shown in the inset) with linear fit (red) of the equilibrium values to determine the electronic DC resistance at 25 °C.

of 60 °C in comparison to room temperature (Figure S5a, Supporting Information), needs to be reduced to negligible values for the application of $MgSc_2Se_4$ as Mg-ion conducting SE. In addition, the zoomed-in view of the high frequency region (0.7–7 MHz) of the Nyquist plot (Figure S5b, Supporting Information) shows no offset of the semicircle, meaning that the ionic conductivity cannot be calculated according to the Jamnik and Maier model done in earlier reports.[16,17,19]

2.3. Verification of Ionic Conductivity

As we explained above, we consider previously reported ionic conductivity data not as reliable due to the insufficient analysis of the impedance data. To provide unequivocal evidence for Mg-ion conduction in $MgSc_2Se_4$, we assembled a Mg|$MgSc_2Se_4$|Au cell with the aim to plate Mg onto the Au electrode at room temperature (current density –428 µAh cm^{-2}). Mg precipitation can only occur if the SE shows Mg-ion conductivity. After the electrochemical experiment, the cell was disassembled, and the Au electrode surface was examined by SEM/EDS. **Figure 3** shows one of the Mg deposits on the backside of the Au electrode, grown from the SE|Au interface through the thin Au layer (300 nm). Magnesium is localized in the deposited particle, while gold and selenium are distributed within the remaining areas (see also Figure S6c,d, Supporting Information). Clearly, the particle is not a contamination from the $MgSc_2Se_4$ pellet. To exclude the possibility of a cross-contamination from Mg particles in the counter electrode, we also checked the morphology of the Mg slurry made from commercial Mg particles, mixed with conductive carbon black (super P) and polyvinylidene fluoride (PVdF) binder. As shown in Figure S7a,b (Supporting Information), the commercial Mg particles inside the mixture are covered with a carbon layer. More importantly, they have a distinctly different morphology (Figure S7c, Supporting Information) compared with the deposited particles, confirming that the Mg particle on the Au surface has been formed by electrochemical plating. This confirms the Mg-ion conductivity of $MgSc_2Se_4$ unequivocally, and to the best of our knowledge, this is the first experimental proof of Mg plating from a Mg-ion SE using an evaporated Au electrode. The thin gas phase deposited electrode has the advantage that the Mg can grow through it, so that a detaching of the electrode to obtain the Mg plating is not necessary. Instead, when using electrode foils, the Mg plating may only be visible at the SE|electrode interface, where contamination of the electrode interface by the SE electrolyte cannot be ruled out, making it difficult to determine the origin of the observed Mg by EDS.[31,32]

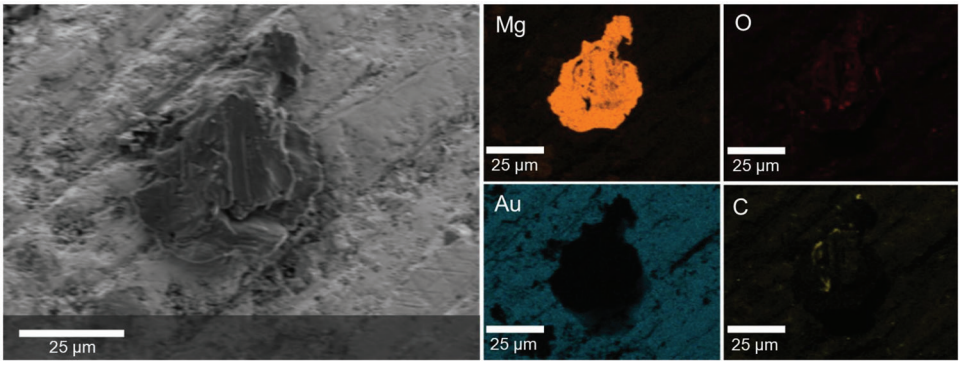

Figure 3. SEM image (left) and elemental EDS maps (right) of deposited Mg on the Au electrode backside, that was grown from the SE|Au interface through the Au layer, after Mg plating in a Mg|$MgSc_2Se_4$|Au cell at 25 °C.

© 2023 The Authors. Advanced Energy Materials published by Wiley-VCH GmbH

16146840, 2023, 40, Downloaded from https://onlinelibrary.wiley.com/doi/10.1002/aenm.202301980 by Cochrane Germany, Wiley Online Library on [07/12/2023]. See the Terms and Conditions (https://onlinelibrary.wiley.com/terms-and-conditions) on Wiley Online Library for rules of use; OA articles are governed by the applicable Creative Commons License

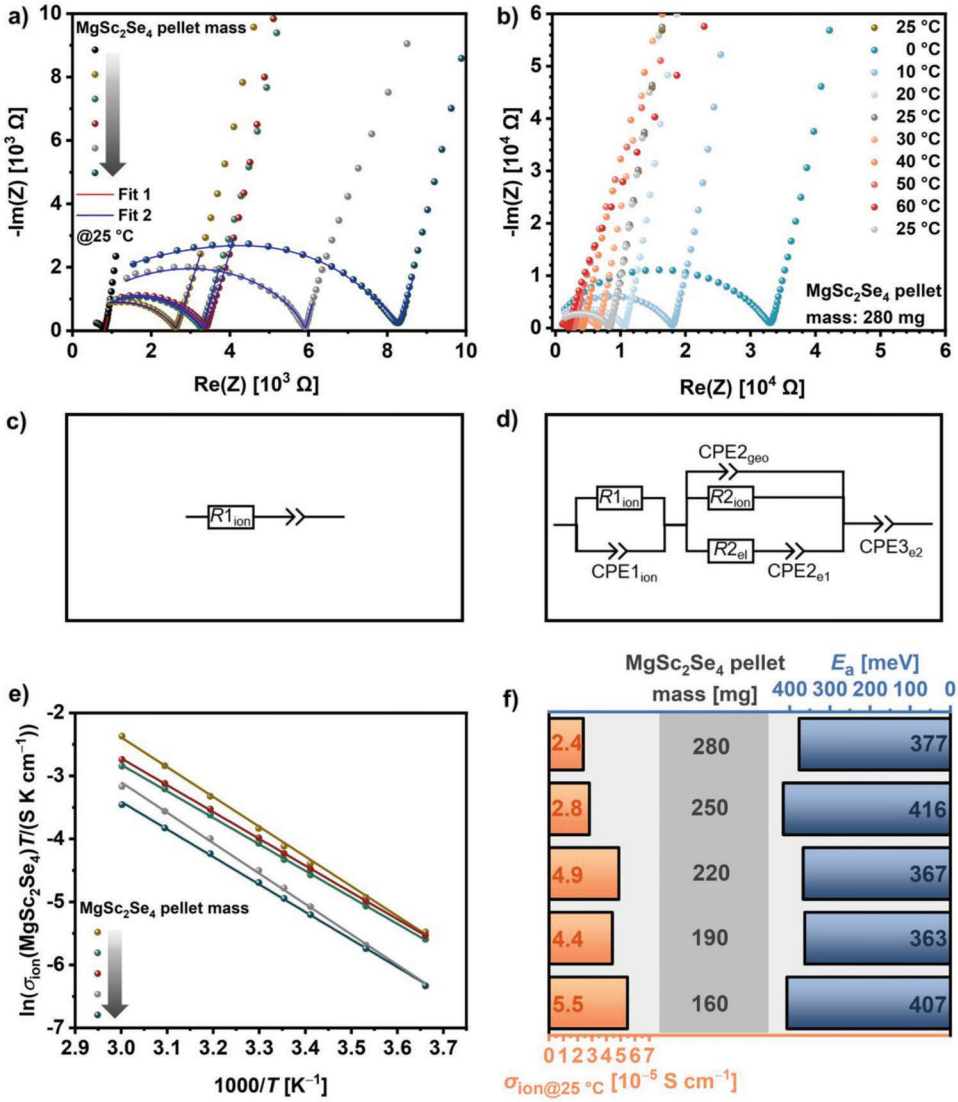

Figure 4. a) Nyquist plots of SS|UiO66-MgIL|$MgSc_2Se_4$|UiO66-MgIL|SS cells at 25 °C with varied spinel pellet mass/thickness (0 mg/0 mm, 160 mg/0.80 mm, 190 mg/0.88 mm, 220 mg/1.10 mm, 250 mg/1.14 mm and 280 mg/1.40 mm) and fits in red and blue; b) Nyquist plots at different temperatures ranging from 0 to 60 °C when a 280 mg spinel pellet is sandwiched; c) and d) equivalent circuits used to fit Nyquist plots for SS|UiO66-MgIL|SS (Fit 1 in a)) and SS|UiO66-MgIL|$MgSc_2Se_4$|UiO66-MgIL|SS cells (Fit 2 in a)); e) Arrhenius plots of the conductivity of $MgSc_2Se_4$ examined from different spinel pellet thicknesses and f) overview of the room temperature ionic conductivity and Mg^{2+} migration barrier calculated by variation of the spinel pellet thickness.

2.4. Ionic Conductivity and Mg^{2+} Migration Barrier

For the measurement of the partial ionic conductivity and the Mg^{2+} migration barrier of $MgSc_2Se_4$, we designed a sandwich-type cell configuration in the before-mentioned press cell and carried out temperature dependent impedance measurements. In detail, Mg-ion conducting interlayers, which block electrons and also improve the electrode/electrolyte contact, are inserted between the cold-pressed $MgSc_2Se_4$ pellet and the stainless-steel ion-blocking electrode (SS|UiO66-MgIL|$MgSc_2Se_4$|UiO66-MgIL|SS). In this case, the Mg-ion conducting ($\sigma_{ion} = 9.5 \times 10^{-5}$ S cm^{-1}) but almost electronically insulating ($\sigma_{el} = 1.7 \times 10^{-10}$ S cm^{-1}, see Figure S8, Supporting Information) UiO66-MgIL electrolyte, based on the Metal-Organic Framework (MOF) structure UiO-66 impregnated with an 1 M $Mg(TFSI)_2$-[EMIM][TFSI] ionic liquid, was used as interlayer.[33] To test the reliability of the chosen method, the $MgSc_2Se_4$ pellet thickness was systematically increased, which should lead to a corresponding proportional increase in the impedance of the cell. The record of the impedance spectra was performed when the impedance in the Nyquist plots at the Re(Z) axis intercept at 25 °C was almost identical, before and after the temperature variation between 0 and 60 °C, meaning the sandwiched system reached equilibrium. Thermal equilibration of the cells took ≈90 min after a temperature step. **Figure 4**a shows the impedance spectra taken at 25 °C for different $MgSc_2Se_4$ pellet thicknesses. The temperature dependent Nyquist plot for the cell with the thickest $MgSc_2Se_4$ pellet (280 mg, 1.40 mm) is exemplified in

© 2023 The Authors. Advanced Energy Materials published by Wiley-VCH GmbH

16146840, 2023, 40, Downloaded from https://onlinelibrary.wiley.com/doi/10.1002/aenm.202301980 by Cochrane Germany, Wiley Online Library on [07/12/2023]. See the Terms and Conditions (https://onlinelibrary.wiley.com/terms-and-conditions) on Wiley Online Library for rules of use; OA articles are governed by the applicable Creative Commons License

16146840, 2023, 40, Downloaded from https://onlinelibrary.wiley.com/doi/10.1002/aenm.202301980 by Cochrane Germany, Wiley Online Library on [07/12/2023]. See the Terms and Conditions (https://onlinelibrary.wiley.com/terms-and-conditions) on Wiley Online Library for rules of use; OA articles are governed by the applicable Creative Commons License

Figure 4b, while the ones of the remaining cells (0, 160, 190, 220 and 250 mg) can be found in Figure S9 (Supporting Information). As expected, the resistance of the semicircle R_{ion}(SEs), representing the total resistance of the two UiO66-MgIL layers and the $MgSc_2Se_4$ pellet, increases with increasing spinel pellet thickness (see Figure 4a). The equivalent circuit shown in Figure 4c was used to describe the impedance of the SS|UiO66-MgIL|SS cell (black plot in Figure 4a), while the semicircle could not be fitted by a constant phase element (CPE) in parallel to the resistance $R1_{ion}$ due to less data points. For $R1_{ion}$ a resistance of 806 Ω, identical with the manually determined resistance of UiO66-MgIL (denoted as R_{ion}(UiO66-MgIL)) from the lowest data point at the intercept of the Re(Z) axis, was obtained. In order to describe the sandwich-type cells, including the $MgSc_2Se_4$ pellet, the physically meaningful equivalent circuit in Figure 4d was applied. The first partial circuit elements, $R1_{ion}$ and $CPE1_{ion}$ belong to the UiO66-MgIL. The following two resistances in parallel, $R2_{ion}$ and $R2_{el}$, represent the two conducting pathways for ions and electrons in the mixed conducting $MgSc_2Se_4$. $CPE2_{geo}$ is a geometric capacitance and the selectively electron-blocking UiO66-MgIL layer is represented by an interface capacitance $CPE2_{e1}$ in the conducting pathways. Finally, $CPE3_{e2}$ describes the ion-blocking stainless-steel electrode. Since the total UiO66-MgIL layer thickness in the cells can deviate from those used in the SS|UiO66-MgIL|SS reference cell (0.60 mm), especially in case of the cell with 220 mg spinel pellet as shown in Table S3 (Supporting Information), R_{ion}(UiO66-MgIL) or $R1_{ion}$, respectively, was adapted to the layer thickness actually used (see Equation S1, Supporting Information). Table S5 (Supporting Information) presents the results of R_{ion}(UiO66-MgIL) and $R1_{ion}$ for each sandwich-type cell. Assuming that the contribution of R_{ion}(UiO66-MgIL) does not cause changes in R_{ion}(SEs) due to constant UiO66-MgIL layer thickness, the impedance of the $MgSc_2Se_4$ can be manually calculated from the difference of both, denoted as $R_{ion}(MgSc_2Se_4)$. Equally, if $R1_{ion}$ is assumed to be constant, $R2_{ion}$, the ionic resistances of $MgSc_2Se_4$ from the fitting, is obtained. Table S5 demonstrates that the results for both, $R_{ion}(MgSc_2Se_4)$ and $R2_{ion}$, are almost identical ($\leq$ 3% derivation $\triangleq \leq 2 \times 10^{-6}$ S cm^{-1}), meaning that fitting of the impedance data in this case is not absolutely necessary. For this reason, $R_{ion}(MgSc_2Se_4)$ was used for all following calculations. Applying Equation 1 to $R_{ion}(MgSc_2Se_4)$, quite close values of the room temperature ionic conductivities for $MgSc_2Se_4$ in the range of $\sigma_{ion}(MgSc_2Se_4) = 2.4–5.5 \times 10^{-5}$ S cm^{-1} (Figure 4f) were found for all cells independent from the interlayer thickness, meaning that the chosen method provides reliable results. At an elevated temperature of 60 °C, an increase of $\sigma_{ion}(MgSc_2Se_4)$ to $9.5 \times 10^{-5} – 2.8 \times 10^{-4}$ S cm^{-1} was observed. From the Arrhenius plots in Figure 4e, the Mg^{2+} migration barrier E_a of $MgSc_2Se_4$ was evaluated from the Arrhenius equation (Equation 2):

$$\sigma_{ion} = \frac{\sigma_0}{T} \exp\left(-\frac{E_a}{k_B T}\right) \quad (2)$$

with σ_0 representing the conductivity prefactor. E_A ranges from 363 to 416 meV for the different cells, being lower than the previously published values for Mg-ion SEs (see Table S6, Supporting Information) and close to the predicted value of 375 meV[16]. All cells operated stably and were reproducible independent from the

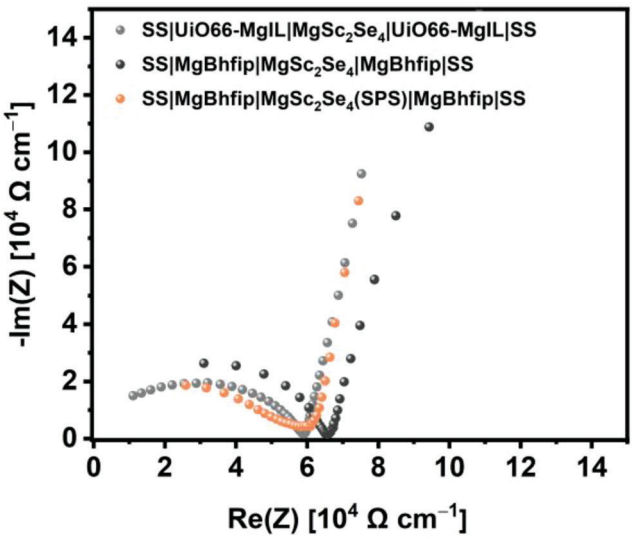

Figure 5. Normalized Nyquist plots of SS|MgBhfip|$MgSc_2Se_4$|MgBhfip|SS cells with sandwiched $MgSc_2Se_4$ pellets (cold-pressed/SPS sintered) showing similar Re(Z) axis intercept resistances compared to a SS|UiO66-MgIL|$MgSc_2Se_4$|UiO66-MgIL|SS cell (with 280 mg $MgSc_2Se_4$ as an example) at 25 °C.

$MgSc_2Se_4$ pellet thickness, confirming the reliability of our cell design with an UiO66-MgIL interlayer.

To check whether the IL from the UiO66-MgIL penetrated the sandwiched spinel pellet, which would influence the resistance of the $MgSc_2Se_4$ pellet, EDS measurements of the pellet cross section were carried out after cell disassembly. Figure S10a (Supporting Information) displays the cross-sectional view of one UiO66-MgIL layer in contact with the sandwiched $MgSc_2Se_4$ with the lowest pellet thickness (0.80 mm) used in this experiment. The element distribution and the spectra of the red labeled areas at the UiO66-MgIL and $MgSc_2Se_4$ layer (Figure S10b,c, Supporting Information) prove that the F, S, and N signals from the IL and $Mg(TFSI)_2$ included in the MOF pores are seen in the corresponding UiO66-MgIL layer but not in the spinel phase. This means that the different layers are chemically well separated and that the results of the EIS measurements are not influenced by diffusion of the IL into pores of the spinel. Furthermore, the unchanged XRD pattern of $MgSc_2Se_4$ powder after soaking it into the IL for one week (Figure S11, Supporting Information) confirms the spinel is chemically stable in contact with the IL.

Apart from the UiO66-MgIL, a 0.1 M $Mg[B(hfip)_4]_2$ liquid electrolyte (hfip = $CH(CF_3)_2$, solvent = 1,2-dimethoxyethane) denoted as MgBhfip[34] was also tested as interlayer. We used the same cell configuration to measure the impedance. Additionally, we also used $MgSc_2Se_4$ pellets prepared by spark plasma sintering (SPS) to increase the pellet density that should prevent penetration of liquid electrolyte (LE). As shown in the corresponding Nyquist plots (Figure S12a,b, Supporting Information), the impedance increased after storage caused by the evaporation of the LE solvent due to insufficiently tight cell housing. However, normalizing the impedance of the very first measurement after cell assembly by the $MgSc_2Se_4$ pellet thickness, quite similar resistances at the Re(Z) axis intercept were obtained (**Figure 5**). The resulting ionic conductivities of 1.9×10^{-5} S cm^{-1} (cold-pressed

© 2023 The Authors. Advanced Energy Materials published by Wiley-VCH GmbH

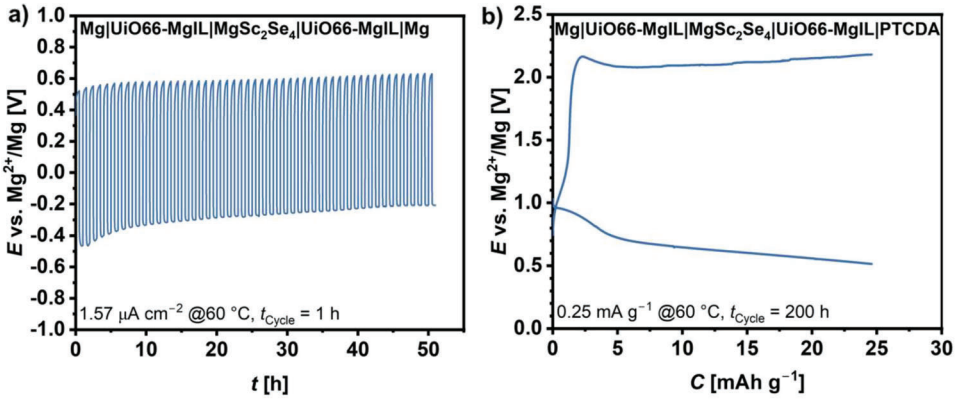

Figure 6. a) 50 cycles of plating/stripping of a Mg|UiO66-MgIL|$MgSc_2Se_4$|UiO66-MgIL|Mg cell at 60 °C by applying a current density of ±1.57 µA cm^{-2} and b) discharge/charge voltage profiles of a Mg|UiO66-MgIL|$MgSc_2Se_4$|UiO66-MgIL|PTCDA full cell at 60 °C by applying current rate of ±0.25 mA g^{-1}.

pellet) and 2.3×10^{-5} S cm^{-1} (SPS pellet), respectively, are slightly smaller than those measured with the UiO66-MgIL interlayer, justified by the fact that the resistances (intercepts) were not reduced by the unknown resistance of the LE-glass fiber layer. Another possibility might be that solvent from the interlayer vaporized already before the measurement. In any case, the quite similar results for the ionic conductivity confirm that the interlayer method can also work with different Mg-ion conducting media and with sintered $MgSc_2Se_4$ pellets instead of cold-pressed powder pellets as well.

Afterwards, symmetrical Mg|UiO66-MgIL|$MgSc_2Se_4$|UiO66-MgIL|Mg cells with Mg foil electrodes were assembled to validate repetitive plating/stripping behavior. Therefore, as shown in **Figure 6**a, 50 cycles at 60 °C were recorded using a current density of 1.57 µA cm^{-2} ($I = 1$ µA). In the initial cycles the symmetrical cell exhibits an overpotential of ≈0.5 V, similar to reported for our Mg|UiO66-MgIL|Mg cell[33]. Upon cycling, the overpotential span decreases and stabilizes, which could be related to the formation of a stable electrode|SE interface. The simultaneous asymmetric overpotential shift in positive direction appears to be due to slightly different surface textures of the both Mg foils caused by manual surface polishing with a knife. However, in general the Mg plating/stripping behavior underlines once more that the spinel indeed shows Mg-ion transport. In the subsequent impedance measurement shown in Figure S13a (Supporting Information), R_{ion}(SEs), the total impedance of the $MgSc_2Se_4$ (m = 120 mg, d = 0.57 mm) and the UiO66-MgIL (m = 120 mg, d = 0.90 mm), was received from the Re(Z) axis intercept in the Nyquist plot. According to the previous procedure, $R_{ion}(MgSc_2Se_4)$ was obtained from the difference of R_{ion}(SEs) and R_{ion}(UiO66-MgIL) (adapted to the actually used layer thickness), and used to calculate the ionic conductivity. The result of 8.9×10^{-5} S cm^{-1} matches well with the previous ones determined with stainless-steel electrodes at 60 °C. This fact demonstrates again the reproducibility of the interlayer method, even when different electrodes (ion-blocking or conducting) are used, since the electrode|SE interface resistance only appears at lower frequencies away from the SEs resistance at higher frequencies.

To demonstrate that $MgSc_2Se_4$ can indeed be used as an electrolyte, a Mg|UiO66-MgIL|$MgSc_2Se_4$|UiO66-MgIL|PTCDA full cell was assembled, including a perylene tetracarboxylic dianhydride (PTCDA) composite cathode, as reported in our earlier work[33]. The galvanostatic discharge and charge profile were recorded at 60 °C in the voltage range between 0.3 and 2.5 V (vs Mg^{2+}/Mg) with a current rate of 0.25 mA g^{-1}. As shown in Figure 6b, the profile exhibits a long plateau in both the discharge and the charge curve, describing the reversible enolization process of the C═O groups in the PTCDA molecule during Mg insertion/extraction. Moreover, a capacity of ≈25 mAh g^{-1} was reached during 100 h of discharge/charge in the first cycle, which is expected to show a strong decay in the following two cycles as reported for the Mg|UiO66-MgIL|PTCDA full cell.[33] However, the results indicate a working battery with $MgSc_2Se_4$ as an electrolyte, and the relative high conductivity of the spinel can be considered as reliably proven.

3. Conclusions

We present unequivocal evidence for Mg-ion transport in the $MgSc_2Se_4$ spinel through a Mg plating experiment. To the best of our knowledge, this is the first report of Mg plating onto a deposited metal electrode from an inorganic Mg-ion SE. In addition, we introduce a straightforward and reliable strategy to determine the partial ionic conductivity ($2.4–5.5 \times 10^{-5}$ S cm^{-1} at room temperature) and the Mg-ion migration barrier of (386 ± 24) meV of the mixed conducting spinel using an electron-blocking UiO66-MgIL interlayer which improves the electrode/electrolyte contact in the press cells and allows high-quality EIS measurements. The migration barrier obtained in the temperature range from 0 to 60 °C agrees well with the one predicted by theory and is lower than the ones published previously for solid-state Mg-ion conductors. Future work will aim to develop a way to reduce the electronic conductivity, which is 0.06–0.14% of the ionic conductivity, or to find less expensive materials as interlayer or coating in order to suppress the undesired electron transport.

4. Experimental Section

Synthesis: Initially, Mg powder (Sigma Aldrich, ≥99%), Sc powder (Chempur, 99.9% REO), and Se powder (Alfa Aesar, 99.999%) were weighted in a molar ratio of 1:2:4 and hand-milled with a mortar for 15 min

© 2023 The Authors. Advanced Energy Materials published by Wiley-VCH GmbH

16146840, 2023, 40, Downloaded from https://onlinelibrary.wiley.com/doi/10.1002/aenm.202301980 by Cochrane Germany, Wiley Online Library on [07/12/2023]. See the Terms and Conditions (https://onlinelibrary.wiley.com/terms-and-conditions) on Wiley Online Library for rules of use; OA articles are governed by the applicable Creative Commons License

for the one-step synthesis of $MgSc_2Se_4$. The resulting powder was isostatically pressed into 0.5 g pellets (Ø = 10 mm) under a pressure of 3000 bar for 30 min. Then, the pellets were wrapped into a platinum foil (Chempur, 99.9%, 125 µm) and placed in separate quartz glass ampules, that were prior heated at 800 °C under dynamic vacuum to remove moisture. After vacuum sealing of the ampules, the solid-state reaction was carried out in a furnace (Nabertherm with controller P 300) at 950 °C for 20 h (180 °C h^{-1} heating rate). Finally, the furnace cooled down to room temperature. After breaking the ampules, the collected pellets were ground to a brownish powder.

Additionally, the synthesis was carried out in a two-step procedure, whereby first MgSe and Sc_2Se_3 were prepared from stoichiometric amounts of the elemental powders according to the previous one-step synthesis at 750 °C for 24 h (180 °C h^{-1} heating rate) and 800 °C for 30 h (60 °C h^{-1} heating rate), respectively. In the next step, the binary compounds were converted to $MgSc_2Se_4$ in a molar ratio of 1:1 at same conditions as described in the first procedure.

All preparations and sample treatments were carried out under an inert gas atmosphere (Ar or vacuum).

X-Ray diffraction (XRD): The binary and ternary selenides were structurally characterized by means of X-ray diffraction using an Empyrean powder diffractometer (Malvern PANalytical Ltd) with Cu K_α radiation. The samples were placed on silicon zero background holders and sealed with Kapton polyimide film inside a glove box to avoid contact with air and humidity. Measurements were carried out in a 2θ range from 10° to 90° with a step size of 0.026° and a counting time per step of 200 s. References were taken from: MgSe (ICSD 53 946), Sc_2Se_3 (ICSD 651 804), and $MgSc_2Se_4$ (ICSD 642 814).

Rietveld Analysis: Rietveld refinements were performed using the software FullProf Suite Version January 2021. The peak profile shape was described by Thompson-Cox-Hasting pseudo-Voigt functions. Start models for the Rietveld refinement were taken from: MgSe (ICSD 53 946) and $MgSc_2Se_4$ (ICSD 642 814).

Scanning Electron Microscopy (SEM) and Energy-Dispersive X-Ray Spectroscopy (EDS): SEM images of the prepared SE powder and pellets were obtained by a Merlin high-resolution scanning electron microscope (Carl Zeiss AG, Germany) at an acceleration voltage of 3 kV. The working distance was between 4 and 5 mm and a secondary electron detector was used. EDS mapping was carried out in 6 mm to 8 mm working distance using an X-Max-50 detector (Oxford Instruments, UK) at an acceleration voltage of 10 kV. Especially, for detection of the Mg deposition on the electrode surface a voltage of 5 kV was used and for the proof of Sc content in the $MgSc_2Se_4$ powder a higher voltage of 15 kV was necessary. For the cross-sectional view, the pellets were manually broken in halves and afterwards attached to the sample holder. The samples were transferred from the glove box with a Leica EM VCT500 shuttle to avoid air contamination.

Transmission Electron Microscopy (TEM): TEM images were obtained by Themis 300 (Thermo Fisher Scientific), which operates at an accelerating voltage of 300 kV. The powder sample was dispersed on the Mo TEM grid for TEM observation. Selected area electron diffraction (SAED) patterns were obtained to identify the crystal structure of the material.

Nuclear Magnetic Resonance (MAS NMR) Spectroscopy: ^{25}Mg and ^{45}Sc magic-angle spinning (MAS) NMR spectroscopy was performed at a magnetic field of 11.7 T corresponding to resonance frequencies of 30.6 and 121.5 MHz, respectively. ^{25}Mg NMR was performed in 1.3 mm rotors at a spinning speed of 22 kHz with a rotor-synchronized Hahn-echo sequence, a $\pi/2$ pulse duration of 3.7 µs, and a recycle delay of 15 s. ^{45}Sc NMR was performed in 2.5 mm rotors at 30 kHz with a Hahn-echo sequence, a $\pi/2$ pulse duration of 2.6 µs, and a recycle delay of 30 s. Spectra were referenced to aqueous solutions of 5 M $MgCl_2$ for ^{25}Mg and 1 M $ScCl_3$ for ^{45}Sc.

Absorption and Photoluminescence Spectroscopy: The $MgSc_2Se_4$ powder was suspended in oil and filled in a fused silica cuvette with a 1 mm optical path length. For µ-reflectance measurements, unpolarized light emitted from a tungsten lamp was utilized and focused onto the sample using a CaF_2 lens. The transmitted light was collected by a 20× objective with a numerical aperture of 0.45, resulting in a 160 µm spot size, and directed into the spectrometer. To obtain absorption spectra, the background intensity (T_{bg}) was subtracted from the sample transmission intensity (T_{sample}) and normalized using the transmission intensity through an identical fused silica cuvette filled with the same oil (T_{ref}). The absorption was calculated as

$$A = 1 - \frac{T_{sample} - T_{bg}}{T_{ref} - T_{bg}} \quad (3)$$

For µ-photoluminescence measurements, the samples were excited using a 532 nm (2.33 eV) laser. The beam was focused by a 20× objective with a numerical aperture of 0.45 into a 3 µm spot size, and the excitation power density was set at 930 W cm^{-2}. The photoluminescence was collected by the same objective and directed into the spectrometer. All optical measurements were carried out at room temperature of 295 K.

Cell Assembly and Electrochemical Measurements: All electrochemical measurements were performed with a VMP300 electrochemical workstation and recorded with the corresponding software EC-Lab from Bio-Logic Science Instruments SAS. Fitting of the experimental EIS data was performed using the RelaxIS 3 software (RHD Instruments, Darmstadt, Germany).

To determine the electronic conductivity, different cell configurations were tested. On the one hand, homemade battery cell casing were used already reported in a previous work[28]. $MgSc_2Se_4$ powder was filled in the PEEK housing with a diameter of 10 mm and pressed between two stainless-steel punches (SS) at 3 t for 3 min to create a pellet inside the housing. When using Ta or Au ion-blocking electrodes, the metal foils (Ø = 9 mm) were subsequently placed between the cold-pressed $MgSc_2Se_4$ pellet and the stainless-steel punches, and the cell was pressed under the same conditions as before. Then, a constant pressure was applied by the means of the screw of aluminum framework around the homemade cell casing with 10 Nm torque, like every time using this cell type. On the other hand, to prepare pouch cells, $MgSc_2Se_4$ powder (300 mg) was pressed into a pellet (Ø = 10 mm) under isostatic pressure of 3000 bar for 30 min. Next, the pellet was vacuum sealed in a quartz glass ampule and sintered at 950 °C for 6 h (180 °C h^{-1} heating rate). After the furnace was cooled down, the pellet was polished down to grit 4000 with SiC sandpaper and Au electrodes of 300 nm thickness (Ø = 8 mm) were vapor-deposited (Sputter Coater, tectra GmbH) on both sides of the $MgSc_2Se_4$ pellet using a 0.15–0.2 nm s^{-1} evaporation rate and a pressure < 10^{-6} mbar. The pellet was again vacuum sintered at 500 °C for 6 h and then sealed under argon into pouch cells using Ni current collectors to contact the Au electrodes. EIS and CA measurements of the symmetrical Me|$MgSc_2Se_4$|Me (Me = stainless-steel, Ta, Au) cells were performed in climate chambers (Weisstechnik) under strict temperature control to prevent errors due to temperature effects. The EIS data were collected from 7 MHz to 100 mHz with an alternating current (AC) amplitude of 10 mV and the CA was carried out in six steps from 0.1 to 2.0 V with 12 h resting time per step. Temperature was varied between −40 and 60 °C.

For the Mg plating experiment with Mg|$MgSc_2Se_4$|Au cells, 500 mg $MgSc_2Se_4$ powder was filled in a graphite pressing tool (Ø = 10 mm) and sintered by the means of spark plasma sintering (SPS) at 3.9 kN and 800 °C for 10 min to a dense pellet (rel. density: 85–91%). Next, the pellet was polished down to grit 4000 with SiC sandpaper and an Au electrode of 300 nm thickness (Ø = 8 mm) was vapor-deposited on one side. After vacuum sintering at 500 °C for 6 h, the other side of the pellet was polished again and coated with a Mg electrode slurry containing Mg powder (Sigma Aldrich, ≥99%), super P (MSE Supplies) and polyvinylidene fluoride (HSV900 PVDF binder, ≥99.5%) binder in a mass ratio of 8:1:1 in *N*-methylpyrrolidone (Sigma Aldrich, 99.5%) which was 77 wt.% of Mg. The coating was then dried at 120 °C for ≈10 min. After storing in Ar-filled glovebox overnight, a pouch cell with Ni current collectors was assembled and chronopotentiometry (CP) with a current of −1 µA for 215 h was used to plate theoretically 97 µg/1.1 µm Mg onto the gold electrode at room temperature.

In order to determine the ionic conductivity and the Mg-ion migration barrier, different amounts of $MgSc_2Se_4$ powder (160, 190, 220, 250, and 280 mg) were pressed in homemade battery cell casing (same procedure as for electronic conductivity). Then, 40 mg of an interlayer was added at both sides of the pellet to prevent electron transport. The interlayer

© 2023 The Authors. Advanced Energy Materials published by Wiley-VCH GmbH

16146840, 2023, 40, Downloaded from https://onlinelibrary.wiley.com/doi/10.1002/aenm.202301980 by Cochrane Germany, Wiley Online Library on [07/12/2023]. See the Terms and Conditions (https://onlinelibrary.wiley.com/terms-and-conditions) on Wiley Online Library for rules of use; OA articles are governed by the applicable Creative Commons License

consisted out of a Mg-ion conducting Metal-Organic Framework (MOF) structure UiO-66 impregnated with 1 M $Mg(TFSI)_2$-[EMIM][TFSI] ionic liquid (magnesium bis (trifluoromethanesulfonyl) imide (TCI, >97%) dissolved in 1-ethyl-3-methylimidazolium bis (trifluoromethanesulfonyl) imide (TCI, >98%)) in a mass ratio of 1:1.25, called UiO66-MgIL as described in the previous report,[33] and was pressed under same conditions as before on the top and bottom side of the $MgSc_2Se_4$ pellet. After applying a pressure by the surrounding aluminum framework with a 10 Nm torque, with all SS|UiO66-MgIL|$MgSc_2Se_4$|UiO66-MgIL|SS cells temperature dependent EIS measurements between 0 and 60 °C were carried out from 3 MHz to 100 mHz with an AC amplitude of 10 mV.

Additionally, instead of the UiO66-MgIL, a LE interlayer was used to sandwich the cold-pressed $MgSc_2Se_4$ pellet (Ø = 10 mm, d = 2.14 mm, 500 mg) or SPS sintered $MgSc_2Se_4$ pellet (Ø = 9.78 mm, d = 1.58 mm, 392 mg), respectively. Therefore, glass fiber separators (Whatman GF/A) with Ø = 10 mm were moistened with one droplet (5 µL) of the $Mg[B(hfip)_4]_2$ LE[34] (0.1 M in 1,2-dimethoxyethane, Sigma Aldrich, 99.5%) and pressed in place of the UiO66-MgIL on both sides of the spinel layer.

Plating/stripping experiments were performed with symmetrical Mg|UiO66-MgIL|$MgSc_2Se_4$|UiO66-MgIL|Mg cells, prepared in an analog procedure mentioned before (see determination of ionic conductivity) with 120 mg $MgSc_2Se_4$ powder and 60 mg UiO66-MgIL per layer. Additionally, polished Mg foils (Sigma Aldrich, 99.9%, 100 µm) with a diameter of 9 mm were placed between the UiO66-MgIL layers and the SS punches. After pressing the cell at 3 t for 3 min, CP was carried out over 50 cycles with alternating plating/stripping times of 30 min for each step and a current of ±1 µA at 60 °C followed by an EIS measurement. The theoretical amount of magnesium plated/stripped on each side is estimated to 11 µg, which corresponds to a homogenous Mg layer of 102 nm.

The cycling experiment was performed with a Mg|UiO66-MgIL|$MgSc_2Se_4$|UiO66-MgIL|PTCDA full cell, prepared similar to the plating/stripping cell, while one of the Mg foils was replaced by a PTCDA composite cathode. The composite was prepared by mixing perylene tetracarboxylic dianhydride powder (PTCDA, Sigma Aldrich, 97%) with UiO66-MgIL and carbon nanofibers (Sigma Aldrich, >98% carbon basis) in a weight ratio of 6:5:1. After cell assembly, galvanostatic cycling was performed at 60 °C in the potential range of 0.3 to 2.5 V with a current of ±0.25 mA g^{-1} and 100 h per discharge/charge step.

Supporting Information

Supporting Information is available from the Wiley Online Library or from the author.

Acknowledgements

This work contributes to the research performed at CELEST (Center for Electrochemical Energy Storage Ulm-Karlsruhe) and was funded by the German Research Foundation (DFG) under Project ID 390874152 (POLiS Cluster of Excellence). The authors would like to thank Ruben Maile (Justus Liebig University) for providing the UiO-66 MOF material, Yushu Tang (KIT) for the TEM measurements and Elisa Monte (Justus Liebig University) for designing the graphical abstract.

Open access funding enabled and organized by Projekt DEAL.

Conflict of Interest

The authors declare no conflict of interest.

Data Availability Statement

The data that support the findings of this study are openly available in Zenodo at https://doi.org/10.5281/zenodo.8209991, reference number 8209991.

Keywords

ceramics, magnesium batteries, $MgSc_2Se_4$, mixed conductors, solid-state electrolytes

Received: June 23, 2023
Revised: August 26, 2023
Published online: September 8, 2023

[1] a) J. Janek, W. G. Zeier, *Nat. Energy* **2016**, *1*, 16141; b) J. T. Frith, M. J. Lacey, U. Ulissi, *Nat. Commun.* **2023**, *14*, 420; c) F. Schipper, D. Aurbach, *Russ. J. Electrochem.* **2016**, *52*, 1095.
[2] F. Liu, T. Wang, X. Liu, L.-Z. Fan, *Adv. Energy Mater.* **2021**, *11*, 2000787.
[3] Y. Liang, H. Dong, D. Aurbach, Y. Yao, *Nat. Energy* **2020**, *5*, 646.
[4] a) L. F. O'Donnell, S. G. Greenbaum, *Batteries* **2021**, *7*, 3; b) M. York, K. Larson, K. C. Harris, E. Carmona, P. Albertus, R. Sharma, M. Noked, E. Strauss, H. Ragones, D. Golodnitsky, *J. Solid State Electrochem.* **2022**, *26*, 1851.
[5] a) H. S. Hirsh, Y. Li, D. H. S. Tan, M. Zhang, E. Zhao, Y. S. Meng, *Adv. Energy Mater.* **2020**, *10*, 2001274; b) N. Yabuuchi, K. Kubota, M. Dahbi, S. Komaba, *Chem. Rev.* **2014**, *114*, 11636.
[6] L. Mei, J. Xu, Z. Wei, H. Liu, Y. Li, J. Ma, S. Dou, *Small* **2017**, *13*, 1701441.
[7] R. Deivanayagam, B. J. Ingram, R. Shahbazian-Yassar, *Energy Storage Mater.* **2019**, *21*, 136.
[8] J. Muldoon, C. B. Bucur, A. G. Oliver, T. Sugimoto, M. Matsui, H. S. Kim, G. D. Allred, J. Zajicek, Y. Kotani, *Energy Environ. Sci.* **2012**, *5*, 5941.
[9] Z. Lu, A. Schechter, M. Moshkovich, D. Aurbach, *J. Electroanal. Chem.* **1999**, *466*, 203.
[10] Y. Zhan, W. Zhang, B. Lei, H. Liu, W. Li, *Front. Chem.* **2020**, *8*, 125.
[11] S. Ikeda, M. Takahashi, J. Ishikawa, K. Ito, *Solid State Ion.* **1987**, *23*, 125.
[12] a) P. W. Jaschin, Y. Gao, Y. Li, S.-H. Bo, *J. Mater. Chem. A* **2020**, *8*, 2875; b) Z. A. Halim, S. Adnan, F. M. Salleh, N. S. Mohamed, *J. Magnes. Alloys* **2017**, *5*, 439.
[13] L. N. Skov, J. B. Grinderslev, A. Rosenkranz, Y.-S. Lee, T. R. Jensen, *Batter. Supercaps* **2022**, *5*, e20220016.
[14] T. Yamanaka, A. Hayashi, A. Yamauchi, M. Tatsumisago, *Solid State Ion.* **2014**, *262*, 601.
[15] a) C. Dietrich, D. A. Weber, S. J. Sedlmaier, S. Indris, S. P. Culver, D. Walter, J. Janek, W. G. Zeier, *J. Mater. Chem. A* **2017**, *5*, 18111; b) M. R. Busche, D. A. Weber, Y. Schneider, C. Dietrich, S. Wenzel, T. Leichtweiss, D. Schröder, W. Zhang, H. Weigand, D. Walter, S. J. Sedlmaier, D. Houtarde, L. F. Nazar, J. Janek, *Chem. Mater.* **2016**, *28*, 6152; c) M. Ghidiu, J. Ruhl, S. P. Culver, W. G. Zeier, *J. Mater. Chem. A* **2019**, *7*, 17735.
[16] P. Canepa, S.-H. Bo, G. Sai Gautam, B. Key, W. D. Richards, T. Shi, Y. Tian, Y. Wang, J. Li, G. Ceder, *Nat. Commun.* **2017**, *8*, 1759.
[17] J. Jamnik, J. Maier, *J. Electrochem. Soc.* **1999**, *146*, 4183.
[18] M. Dillenz, M. Sotoudeh, C. Glaser, J. Janek, A. Groß, H. Euchner, *Batter. Supercaps* **2022**, *5*, e202200164.
[19] L.-P. Wang, Z. Zhao-Karger, F. Klein, J. Chable, T. Braun, A. R. Schür, C.-R. Wang, Y.-G. Guo, M. Fichtner, *ChemSusChem* **2019**, *12*, 2286.
[20] a) S. Kundu, N. Solomatin, Y. Kauffmann, A. Kraytsberg, Y. Ein-Eli, *Appl. Mater. Today* **2021**, *23*, 100998; b) S. Kundu, N. Solomatin, A. Kraytsberg, Y. Ein-Eli, *Energy Tech.* **2022**, *10*, 2200896.
[21] H. Rickert, in *Inorganic Chemistry Concepts*, (Eds.: C. K. Jørgensen, M. F. Lappert, S. J. Lippard, J. L. Margrave, K. Niedenzu, H. Nöth, R. W.

© 2023 The Authors. Advanced Energy Materials published by Wiley-VCH GmbH

16146840, 2023, 40, Downloaded from https://onlinelibrary.wiley.com/doi/10.1002/aenm.202301980 by Cochrane Germany, Wiley Online Library on [07/12/2023]. See the Terms and Conditions (https://onlinelibrary.wiley.com/terms-and-conditions) on Wiley Online Library for rules of use; OA articles are governed by the applicable Creative Commons License

Parry, H. Yamatera, H. Rickert), Springer, Berlin, Heidelberg, **1982**, pp. 79–117.
[22] A. Senocrate, I. Moudrakovski, G. Y. Kim, T.-Y. Yang, G. Gregori, M. Grätzel, J. Maier, *Angew. Chem.* **2017**, *129*, 7863.
[23] a) I. Riess, *Solid State Ionics* **1991**, *44*, 207; b) W. Weppner, R. A. Huggins, *Annu. Rev. Mater. Sci.* **1978**, *8*, 269.
[24] P. Canepa, G. Sai Gautam, D. Broberg, S.-H. Bo, G. Ceder, *Chem. Mater.* **2017**, *29*, 9657.
[25] a) K. D. Pham, M. Batouche, D. S. Mohammed, T. Seddik, T. V. Vu, D. D. Vo, N. N. Hieu, O. Y. Khyzhun, *J. Solid State Chem.* **2021**, *293*, 121763; b) W. Tahir, G. M. Mustafa, N. A. Noor, S. M. Alay-e-Abbas, Q. Mahmood, A. Laref, *Ceramics Int.* **2020**, *46*, 26637.
[26] W. M. Yim, A. K. Fan, E. J. Stofko, *J. Electrochem. Soc.* **1973**, *120*, 441.
[27] M. Guittard, C. Souleau, H. Farsam, *C. R. Hebd. Acad. Sci.* **1964**, *259*, 2847.
[28] W. Zhang, D. A. Weber, H. Weigand, T. Arlt, I. Manke, D. Schröder, R. Koerver, T. Leichtweiss, P. Hartmann, W. G. Zeier, J. Janek, *ACS Applied Mater. Interfaces* **2017**, *9*, 17835.
[29] Y. Gao, T. P. Mishra, S.-H. Bo, G. Sai Gautam, P. Canepa, *Annu. Rev. Mater. Res.* **2022**, *52*, 129.
[30] J. Zahnow, T. Bernges, A. Wagner, N. Bohn, J. R. Binder, W. G. Zeier, M. T. Elm, J. Janek, *ACS Appl. Energy Mater.* **2021**, *4*, 1335.
[31] E. Roedern, R.-S. Kühnel, A. Remhof, C. Battaglia, *Sci. Rep.* **2017**, *7*, 46189.
[32] K. Kisu, S. Kim, M. Inukai, H. Oguchi, S. Takagi, S. Orimo, *ACS Appl. Energy Mater.* **2020**, *3*, 3174.
[33] Z. Wei, R. Maile, L. M. Riegger, M. Rohnke, K. Müller-Buschbaum, J. Janek, *Batter. Supercaps* **2022**, *5*, e202200318.
[34] Z. Zhao-Karger, R. Liu, W. Dai, Z. Li, T. Diemant, B. P. Vinayan, C. Bonatto Minella, X. Yu, A. Manthiram, R. J. Behm, M. Ruben, M. Fichtner, *ACS Energy Lett.* **2018**, *3*, 2005.

© 2023 The Authors. Advanced Energy Materials published by Wiley-VCH GmbH

16146840, 2023, 40, Downloaded from https://onlinelibrary.wiley.com/doi/10.1002/aenm.202301980 by Cochrane Germany, Wiley Online Library on [07/12/2023]. See the Terms and Conditions (https://onlinelibrary.wiley.com/terms-and-conditions) on Wiley Online Library for rules of use; OA articles are governed by the applicable Creative Commons License